FINAL REPORT

Date: March 1, 1999

Award Number: 1434-HQ-96-GR-02736

Title: The 1993 Klamath Falls, Oregon, Earthquake Sequence: Implications for Normal Fault Interactions and Segmentations

Principal Investigator: John Nabelek
College of Oceanic and Atmospheric Sciences
Oregon State University
Corvallis, OR 97331

SUMMARY

The 1993 Klamath Falls, Oregon, earthquake sequence is characterized by two magnitude 6.0 mainshocks. Although the Klamath Falls region is in the immediate backarc of the Cascadia volcanic arc, tectonically it represents the extreme northwestern part of the Basin and Range province. The mainshocks were preceded by a foreshock and a very vigorous, long-term aftershock sequence. The data from the permanent broadband and short-period regional networks have been analyzed. The complicated evolving pattern of epicenters and fault-plane solutions indicates that the earthquakes occurred on a segmented web of faults interacting with each other at various time scales. Resolution of the details of this sequence, particularly during the first few weeks following the strong events, before permanent stations were established in the epicentral area, is limited due to inadequate regional network coverage. The purpose of this project was to analyze data from 23 temporary digital and analog stations deployed in the epicentral region a few hours after the mainshocks. Incorporating these data would improve our ability to locate earthquakes in the early part of the sequence. This information, combined with focal mechanisms, would enable us to better resolve the mainshocks' causative faults and their geometry, and thus to better understand the factors influencing rupture initiation and termination. It would also help us to improve our understanding of processes involved in spreading of the aftershock activity from one fault to another. The grant also provided funds for completion of the study of aftershocks of the March 1993, Scotts Mills, Oregon, earthquake (M_w=5.6), a study initiated by a small USGS grant 1434-94-G-2427.

The compilation and analysis of the Klamath Falls aftershock data was much more time consuming than originally anticipated. Merging of the data sets collected by the various field crews turned out to be very labor intensive and therefore we submitted a proposal requesting a second-year extension on this grant. The proposal was highly rated by the peer-review panel, however, the request was put on hold pending availability of funds. Unfortunately, sufficient funds to complete this study did not become available. Facing the disappointing outcome we decided to focus on the Scotts Mills study, which was showing very promising preliminary results.

The following is an abstract of an article submitted to the Geophysical Journal International: We analyzed aftershocks recorded by a temporary digital seismic network

following the moderate $M_w = 5.5$, 1993, Scotts Mills, Oregon earthquake. A technique to retrieve source moment tensors from local waveforms was developed, tested, and applied to 41 small earthquakes (M_w ranging from 1.6 to 3.2). The derived focal mechanisms, although well resolved, are highly variable and do not share a common nodal plane. On the other hand, a majority of the events, relocated with a *Joint Hypocenter Determination* algorithm collapsed to a well-focused plane. The incompatibility of most events' nodal planes with the plane defined by their locations, suggests that the aftershocks did not occur on the fault plane, but tightly around it, outlining the rupture area rather than defining it. Furthermore, the moment tensors reveal stable P-axes, whereas T-axes plunges are highly dispersed. We detect a rotation of average T-axis plunge with depth, indicating a change from shallower, predominantly dip-slip mechanisms to deeper strike-slip mechanisms. These characteristics are difficult to explain by remnant stress concentrations on the mainshock rupture plane or asperity- and barrier-type models. We suggest the aftershocks occurred under the ambient regional stress, triggered by a sudden weakening of the region surrounding mainshock slip, rather than from a shear stress increase due to the mainshock.

TECHNICAL DETAILS

In lieu of the technical report, we provide the galley proofs of the paper entitled "New techniques for the analysis of earthquake sources from local array data with an application to the 1993 Scotts Mills, Oregon, aftershock sequence", which will be published in the Geophysical Journal International.

STUDENT SUPPORT

This grant supported two graduate students, Beate Leitner, who worked with the Kalmath falls data, and Bernd Schurr, who worked with the Scotts Mills data. Bernd Schurr's work resulted in a Masters Thesis, AGU presentation, and an article in a peer-reviewed journal.

PUBLICATIONS, THESES AND ABSTRACTS

Schurr, B., The 1993, Scotts Mills, Oregon, Aftershock Sequence: Moment Tensor Inversion and Joint Hypocenter Determination, M.S. thesis, OSU, December, 1996.

Schurr, B., and J. Nabelek, The 1993, Scotts Mills, Oregon, Aftershock Sequence: Moment Tensor Inversion and Joint Hypocenter Determination, *EOS*, 1996.

Schurr, B., and J. Nabelek, New techniques for the analysis of earthquake sources from local array data with an application to the 1993 Scotts Mills, Oregon, aftershock sequence, *Geophys. J. Int.*, *136*, 1999.

Geophys. J. Int. (1999) **136**, 000–000

New techniques for the analysis of earthquake sources from local array data with an application to the 1993 Scotts Mills, Oregon, aftershock sequence

Bernd Schurr* and John Nábělek

College of Oceanic and Atmospheric Sciences, Oregon State University, Corvallis, OR 97331, *USA. E-mail: nabelek@oce.orst.edu*

Accepted 1998 October 14. Received 1998 June 10; in original form 1997 July 30

SUMMARY

We analysed aftershocks recorded by a temporary digital seismic network following the moderate $M_w = 5.51993$, Scotts Mills, Oregon earthquake. A technique to retrieve source moment tensors from local waveforms was developed, tested, and applied to 41 small earthquakes (M_w ranging from 1.6 to 3.2). The derived focal mechanisms, although well resolved, are highly variable and do not share a common nodal plane. In contrast, however, the majority of the events, relocated with a joint hypocentre determination algorithm, collapse to a well-focused plane. The incompatibility of the nodal planes of most events with the plane defined by their locations suggests that the aftershocks did not occur on the fault plane, but tightly around it, outlining the rupture area rather than defining it. Furthermore, the moment tensors reveal stable *P*-axes, whereas *T*-axes plunges are highly dispersed. We detect a rotation of average *T*-axis plunge with depth, indicating a change from shallower, predominantly dip-slip mechanisms to deeper strike-slip mechanisms. These characteristics are difficult to explain by remnant stress concentrations on the main-shock rupture plane or asperity- and barrier-type models. We suggest that the aftershocks occurred under the ambient regional stress, triggered by a sudden weakening of the region surrounding the main-shock slip, rather than from a shear stress increase due to the main shock.

Key words: aftershocks, earthquakes, joint hypocentre determination, moment tensor inversion.

INTRODUCTION

Despite the widespread availability of digital three-component data, the commonly used technique to estimate fault orientation and slip direction of small earthquakes is still the mapping of first-motion polarities. While waveform inversion techniques have been proved to give reliable estimates of source parameters, even with sparse station coverage, and are now routinely employed to obtain source parameters from long-period body and surface waves recorded at teleseismic and regional distances (for example Dziewonski *et al.* 1983; Nábělek 1984; Ritsema & Lay 1993; Dreger & Helmberger 1993; Nábělek & Xia 1995), applications to short-period data from local earthquakes are rare (for example Saikia & Herrmann 1985, 1986; Koch 1991a, 1991b; Sileny *et al.* 1992; Mao *et al.* 1994). Large and moderate earthquakes can be analysed at sufficiently low frequencies (<0.1 Hz) that seismograms even at distant stations can be modelled with relatively simple velocity models. Small earthquakes have to be analysed at much higher frequencies (>0.5 Hz) for the signal to emerge from the ambient noise. At very close range (epicentral distance ≤ depth), the use of simple crustal models is still possible even at such high frequencies because there the direct *P* and *S* arrivals are dominant. Their waveforms are simple and robust, and can be modelled even if the structure of the region under study is not well known. Accordingly, *P* and *S* waves are well suited for source-mechanism determinations in aftershock studies using local digital recordings.

In this paper we adapt a technique routinely used for regional waveform modelling in the Pacific Northwest (Nábělek & Xia 1995), and apply it to near-source data of aftershocks of the $M_w = 5.5$, 1993 March 25 Scotts Mills, Oregon, earthquake. The Scotts Mills and Klamath Falls earthquakes in 1993 were the largest to have occurred in Oregon in over a hundred years (for example Nábělek & Xia 1995; Braunmiller *et al.* 1995). The Scotts Mills event occurred at a shallow depth (approximately 15 km) in the forearc of the Cascadia subduction zone (Fig. 1). Teleseismic and regional waveforms (Nábělek & Xia 1995), as well as *P*-wave polarities (Thomas *et al.* 1996), revealed an oblique mechanism with approximately equal amounts of reverse and strike-slip motion (Fig. 1).

* Now at: GeoForschungsZentrum Potsdam, 14473 Potsdam, Germany.

© 1999 RAS

gp00000771 23-12-98 08:41:03 Rev 14.05
The Charlesworth Group, Huddersfield 01484 517077

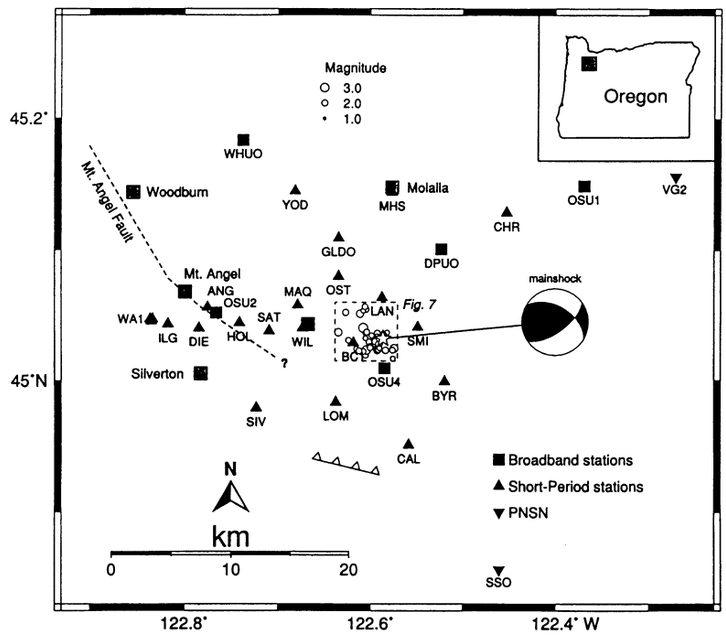

Figure 1. Map of the epicentral region of the 1993 Scotts Mills earthquake. Shown are: seismic network (labels with capital letters), locations of aftershocks (circles), and the main shock (star). The fault-plane solution of the main shock (beach ball, strike = 302°, dip = 51°, rake = 145°; depth = 12.5 km; $M_w = 5.5$) was determined by Nábělek & Xia (1995) from regional long-period waveforms. The dashed line is the mapped trace of Mt Angel Fault, the barbed line the surface projection of the aftershock plane. The region covered in Fig. 7 is indicated.

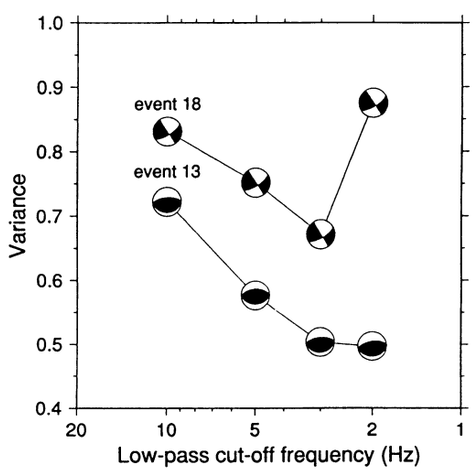

Figure 2. Low-pass-filter cut-off versus variance of fit (normalized by the power of the data) of the moment tensor solution. For display purposes, 0.2 was added to the variances of event 18.

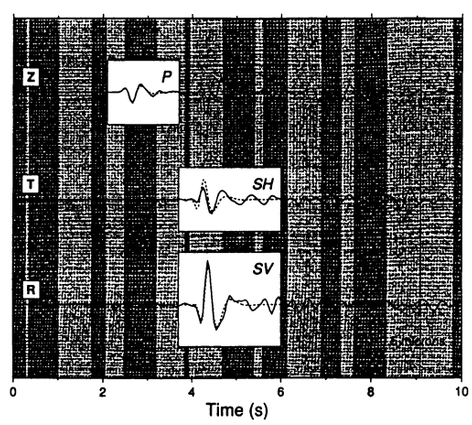

Figure 3. Schematic view of the moment tensor inversion windows. Only the highlighted parts of the seismograms are used in the analysis. Observed (solid line) and synthetic (dashed line) seismograms are aligned and weighted separately in each window.

gp00000771 23-12-98 08:41:03 Rev 14.05
The Charlesworth Group, Huddersfield 01484 517077

The relatively modest aftershock sequence was exceptionally well recorded by a temporary array of 28 three-component, digital seismographs. Using these data we relocated and determined moment tensors for 41 of the larger aftershocks ranging in magnitude (M_d) from 0.8 to 3.2. In this paper we will describe the moment tensor inversion and relocation method, determine the stress regime from the moment tensors, and then discuss the findings in the context of aftershock generation.

DATA

Hours after the main shock, teams from the US Geological Survey, University of Oregon, and Oregon State University deployed 22 three-component short-period (2 Hz, Mark Products L-22 and Sprengnether S6000) and six broad-band seismographs (0.01–25 Hz STS-2, 0.03–25 Hz CMG-3ESP) in the epicentral area. The short-period seismograph deployment is described by Thomas *et al.* (1996). The network had an excellent coverage of the epicentral region (Fig. 1). During a period of about three weeks, approximately 180 aftershocks were recorded. All seismograms were converted into ground displacement by correcting for instrument response, and later filtered into appropriate passbands as discussed below.

FOCAL MECHANISMS

Method

There have been only a few attempts to invert high-frequency waveforms of small local earthquakes for their source parameters (Saikia & Herrmann 1985, 1986; Koch 1991a; Sileny *et al.* 1992). These analyses utilizing entire waveforms were

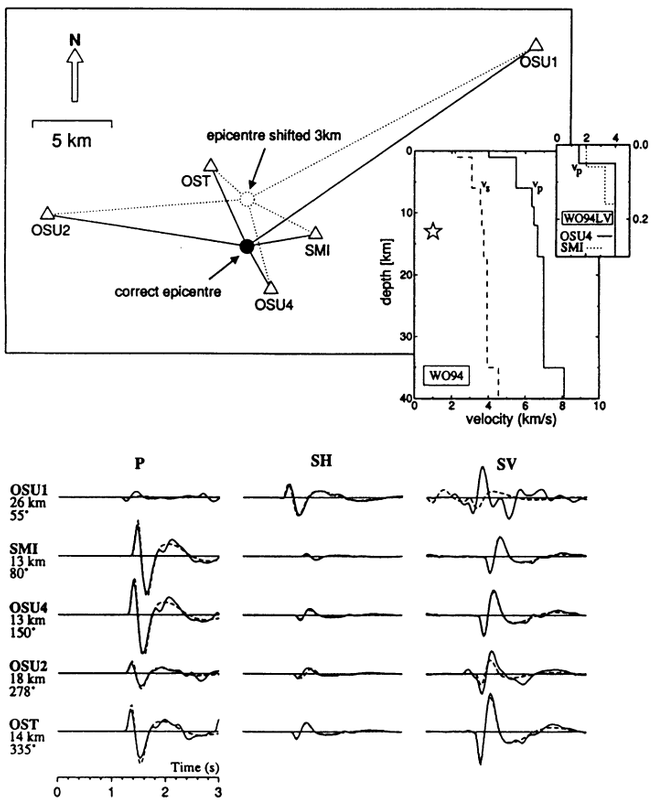

Figure 4. Top: Set-up of the synthetic experiment conducted to investigate the effect of simplified earth models and mislocated epicentres on the inversion. The dotted line depicts the change in event-station geometry if the epicentre is erroneously shifted 3 km to the north. The velocity models WO94 and WO94LV were used to calculate 'observed' seismograms, and the star indicates the event depth. Bottom: Comparison of seismograms for a homogeneous half-space (dashed lines) with seismograms for model WO94 (solid lines), displaying the influence of crustal layering. Except for the radial component at the most distant station OSU1, the effect of crustal layering on the near-source seismograms is only secondary. In this comparison, a dip-slip source with the correct epicentre was used.

© 1999 RAS, *GJI* 136, 000–000

gp00000771 23-12-98 08:41:03 Rev 14.05
The Charlesworth Group, Huddersfield 01484 517077

hampered by velocity models that proved inadequate in simulating high frequencies. To overcome the complexities encountered in waveform inversions, Schwartz (1995) used *P* and *S* amplitude ratios, at the expense of increasing the non-uniqueness of the solutions.

Our procedure differs in two important ways from earlier methods: (1) we band-limit the data and synthetics to frequencies where displacement waveforms become simple, distinct, pulse-like direct *P* and *S* arrivals, little contaminated by other crustal phases; and (2) we model *P*, *SV*, and *SH* phases in separate windows, wherein they are allowed to align independently. These two modifications contribute immensely to the robustness of the method.

We found band-pass filtering to be crucial in our effort to model the observed arrivals. The high-pass cut-off is set by the signal power at low frequencies, whereas our ability to simulate the observed data determines the low-pass cut-off. Fig. 2 shows normalized variance, a measure of fit, and focal mechanisms from inversions in frequency bands with the low-pass cut-off decreasing from 10 to 2 Hz for two events (13 and 18). The match between observed seismograms and synthetics improves as the waveforms become simpler at lower frequencies. At low frequencies, the variance curve flattens (event 13) or increases again (event 18) because of the lack of signal power. Although the double-couple estimate is fairly stable over the range of pass bands, we found the band between 0.5 and 3.0 Hz to be the most suitable (Fig. 2). In general the appropriate passband will depend on the knowledge of crustal structure, microseismic noise levels, and data quality.

Information necessary for determining the earthquake moment tensor is contained in the direct *P*, *SH* and *SV* pulses recorded, respectively, on the *Z* (vertical), *T* (transverse), and *R* (radial) components. The R component of *P* and the *Z* component of *SV* are not used because they are less stable and likely to be contaminated by difficult-to-predict converted phases, near-surface effects and small variations in take-off angles (Fig. 3). Within each window, we allow for appropriate alignment of the observed and theoretical waveforms. Independent alignment of *P* and *S* phases is crucial because the 1-D velocity model used in generating the synthetics cannot account for exact arrival times for both phases at all

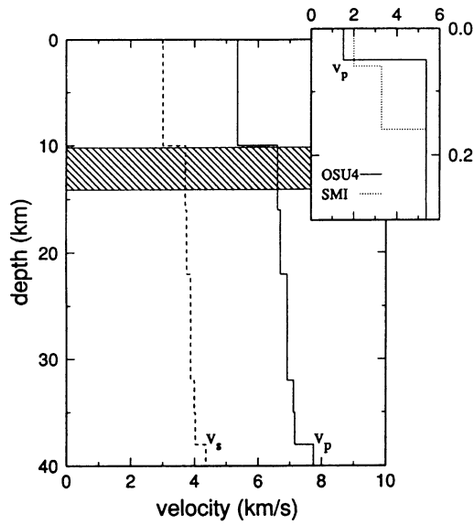

Figure 5. The velocity model of Thomas *et al.* (1996) used for the single-event locations and to calculate Green's functions for the moment tensor inversion of actual data. At stations OSU4 and SMI, shallow, low-velocity layers were introduced to model anomalously high amplitudes and reverberations. The hatched band indicates the depth range of the aftershocks. The up-going rays, dominant near the epicentre, are influenced only by the upper two layers.

Table 1. Results of synthetic testing.

Model Syn	Model Obs	Source [DS/SS]	SV [+/−]	Strike/Dip/Rake [°]	M_0	DC [%]
HS	WO94	DS	−	90.5/45.2/90.3	1.03	94.4
		DS	+	90.6/45.1/90.5	1.11	82.4
		SS	−	133.7/87.5/179.5	1.10	97.3
		SS	+	45.5/89.2/358.3	1.12	99.6
	WO94LV	DS	−	89.3/45.7/86.2	1.08	88.6
		DS	+	92.1/44.2/90.9	1.34	73.3
		SS	−	45.5/87.9/0.3	1.14	99.4
		SS	+	45.8/84.9/359.4	1.25	96.7
HS-ML	WO94	DS	−	86.2/52.8/82.1	0.92	57.9
		DS	+	85.7/51.8/83.5	1.00	56.8
		SS	−	314.6/76.7/192.5	0.96	89.3
		SS	+	315.1/76.8/190.7	1.01	89.2
	WO94LV	DS	−	90.2/53.9/77.4	0.96	41.6
		DS	+	89.5/49.6/85.3	1.26	45.4
		SS	−	317.9/71.8/191.1	0.96	88.8
		SS	+	317.5/73.5/188.0	1.07	94.0

Model Syn and Model Obs: crustal models used to calculate synthetic and 'observed' seismograms. HS: half-space with average velocity (5.8 km s^{-1}) of WO94. HS-ML: half-space with event misplaced 3 km to the north. WO94: layered velocity model of Fig. 4. WO94LV: same model as WO94 with a low-velocity top included (see inset Fig. 4). DS: dip-slip source with strike = 90°, dip = 45°, and rake = 90°. SS: strike-slip source with strike = 45°, dip = 90°, and rake = 0°. M_0: seismic moment normalized by the true moment. SV: '−' if SV phase was excluded, '+' if SV was included in inversion. Strike/Dip/Rake—of best-DC inversion solution. DC: double-couple portion of moment tensor.

gp00000771 23-12-98 08:41:03 Rev 14.05
The Charlesworth Group, Huddersfield 01484 517077

recording stations, yet even a minor error in the predicted traveltime causes a misalignment between observed and synthetic seismograms which severely biases the solution. The separate windowing additionally enables different weighting of *P* and *S* phases.

The principle behind the moment tensor inversion technique is described by Nábělek & Xia (1995). Although implemented in our computer code, we do not invert for the source time history but use a step function. For earthquakes of such small size ($M_w \leq 3.0$), corner frequencies higher than 10 Hz are expected (Brune 1970, 1971), and the source time function is not well resolvable in the frequency band considered. Excitation functions are calculated using a discrete wavenumber summation technique (Bouchon 1982). The moment tensor is constrained to be purely deviatoric. We refer to its double-couple (DC) and compensated linear vector dipole (CLVD) components as defined by Dziewonski *et al.* (1981). The seismic moments quoted represent the strength of the DC.

Synthetic tests

The least-squares solution to the inverse problem is unbiased if the data are contaminated by additive, normally distributed noise. However, the effect of inaccurate Green's functions due to uncertainties and simplifications in crustal models and mislocated hypocentres is more difficult to assess. To gauge the susceptibility of the inversion estimates to these sources of error, tests with synthetic data were conducted. Synthetic

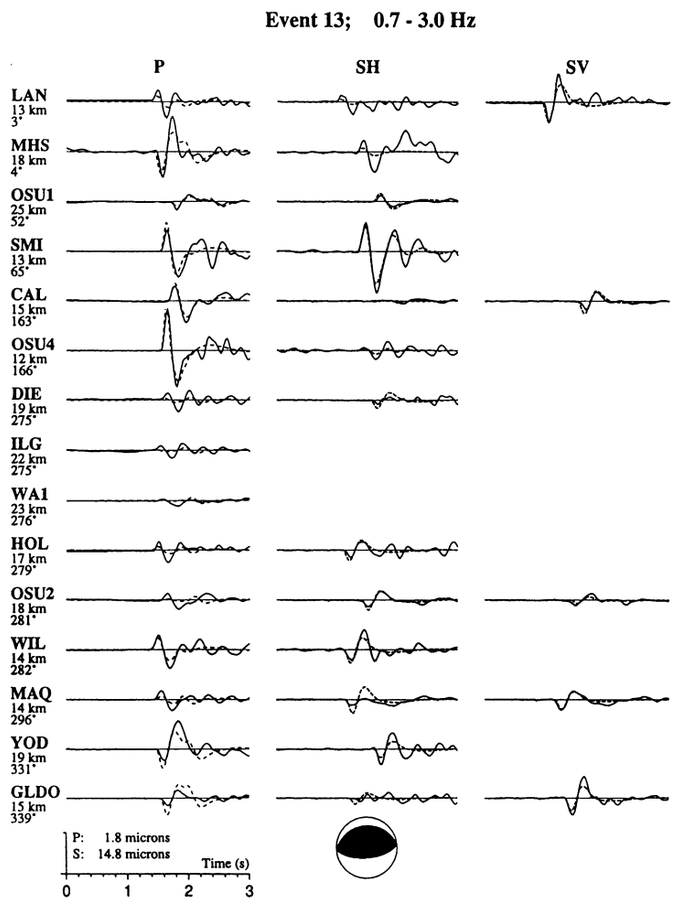

Figure 6. Observed and best-fit synthetic seismograms (ground displacement) for a $M_w = 2.6$ reverse-faulting event (13) and a $M_w = 2.2$ strike-slip-faulting event (18). Below the station names, hypocentral distances and backazimuths are given. The beach ball describes the double couple obtained in the inversion. Source parameters are listed in Table 2.

© 1999 RAS, *GJI* 136, 000–000

gp00000771 23-12-98 08:41:03 Rev 14.05
The Charlesworth Group, Huddersfield 01484 517077

seismograms for a subset of five stations with coordinates from the temporary array were calculated for a dip-slip and strike-slip source buried at 13 km depth in a layered crust (WO94 and WO94LV in Fig. 4), and subsequently used as observed ones. Synthetics from a homogeneous half-space velocity model were then used to retrieve source parameters. Results for different test scenarios are summarized in Table 1.

In a first experiment, designed to gauge the effect of inaccuracies in crustal structure, we retrieve source parameters using excitation functions calculated for a homogeneous half-space (HS in Table 1) having an average velocity of the original layered model. Fig. 4 shows the station distribution and observed and synthetic seismograms. Despite the grossly simplified 'assumed' crustal model, the inversion perfectly recovers the source DC, but erroneously introduces up to 18 per cent CLVD in the moment tensor, and slightly overestimates the moment. For the steeply departing rays, recorded at the near stations, the effect of impedance discontinuities is only secondary, reflection and conversion amplitudes are small, and energy partitioning at the free surface is well modelled by the half-space synthetics. In contrast, the observed *SV* waveforms at the more remote stations become dominated by complex wave interactions in the layered crust, causing a complete mismatch between observed and synthetic seismograms at the most distant station OSU1. Guided by this observation, we model the *SV* phase only at close stations, where waveforms are simple enough to be modelled by a gross earth model. The inclusion of an anomalous low-velocity near-surface layer beneath two stations (WO94LV in Table 1, Fig. 4) affects the moment and CLVD content but not the source orientation.

Hypocentral location errors cause timing errors and change the event–receiver geometry, thereby biasing the radiation pattern. In our method the timing errors are removed by aligning synthetic and observed *P* and *S* seismograms. Changes in geometry, however, can be significant for stations in the

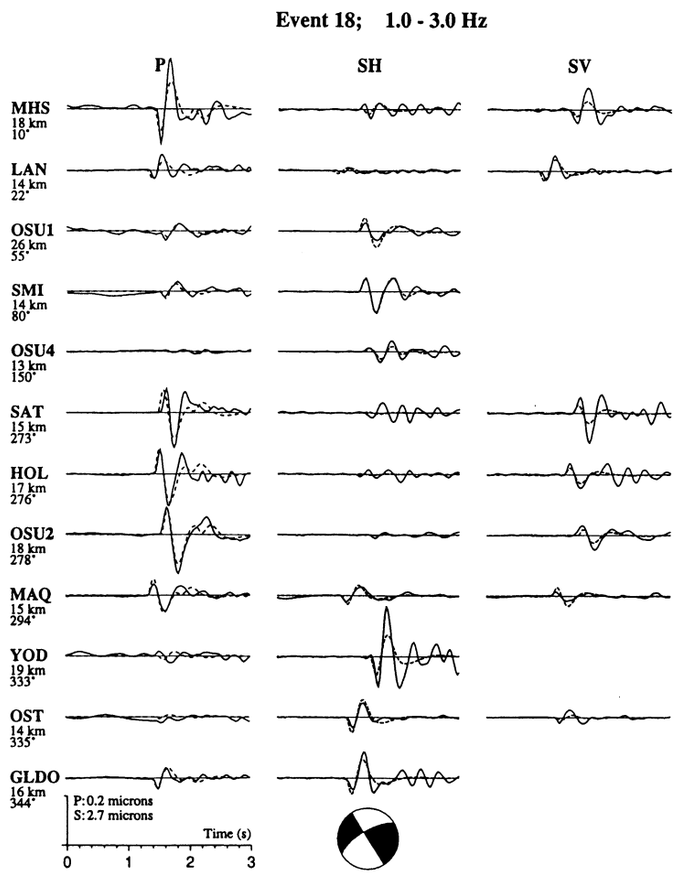

Figure 6. (*Continued.*)

gp00000771 23-12-98 08:41:03 Rev 14.05
The Charlesworth Group, Huddersfield 01484 517077

proximity of the epicentres. To investigate these effects, the source was misplaced 3 km north of its correct location, severely changing the event-station geometry (Fig. 4). The parameters of the recovered DCs differ from the correct ones by as much as 13° (Table 1), yet the general type of faulting is still well retrieved, and most of the mismatch appears to be absorbed by the CLVD component of the moment tensor. For our data, we estimate location errors of only a few hundred metres; hence the effect of the source mislocation on the estimated moment tensor is minor. However, in situations where the location uncertainties are larger, this effect should be considered.

All tests indicate that the method is remarkably insensitive to inaccurate Green's functions. Misfit between data and synthetics is often projected into the CLVD component of the moment tensor, leaving the DC parameters strike, dip, and rake relatively undisturbed.

Application to the Scotts Mills sequence

The moment tensor inversion was applied to 41 aftershocks of the Scotts Mills sequence recorded by at least three and at most 15 stations of the temporary network. Excitation functions were computed using the crustal model from Thomas *et al.* (1996) (Fig. 5). At stations OSU4 and SMI, shallow layers of low seismic speed were added to model high amplitudes and strong reverberations from underlying sediments. The thickness and velocity of these thin layers were found by crude modelling of the amplitude and phase of first and multiple arrivals. The event locations used for the moment-tensor analysis were computed using both the temporary and regional stations as discussed in more detail later.

Fig. 6 shows observed and best-fit theoretical seismograms for two representative events. The three phases show large variations in amplitudes over azimuth, and constrain the radiation pattern of the source well. In the chosen frequency band, data are relatively simple, and generally well matched by the synthetics.

Fig. 7 shows lower-hemisphere fault-plane solutions of all 41 events analysed in this study mapped onto the JHD epicentres presented later. The source parameters for all events are summarized in Table 2. The earthquake sequence exhibits a remarkable variability in source mechanisms. Such non-uniformity in focal mechanisms is not expected for aftershocks if they are believed to occur on a common fault plane in the aftermath of the main shock. We present several examples demonstrating that the differences in mechanisms are not caused by a lack of resolution or by artefacts introduced by the recording geometry.

Resolution

First we present a simple qualitative example. Fig. 8 shows seismograms of two small events (event 38, $M_w = 1.84$, and event 39, $M_w = 1.86$; Table 2) separated by five hours on 1993 April 1. Both events occurred at about the same location,

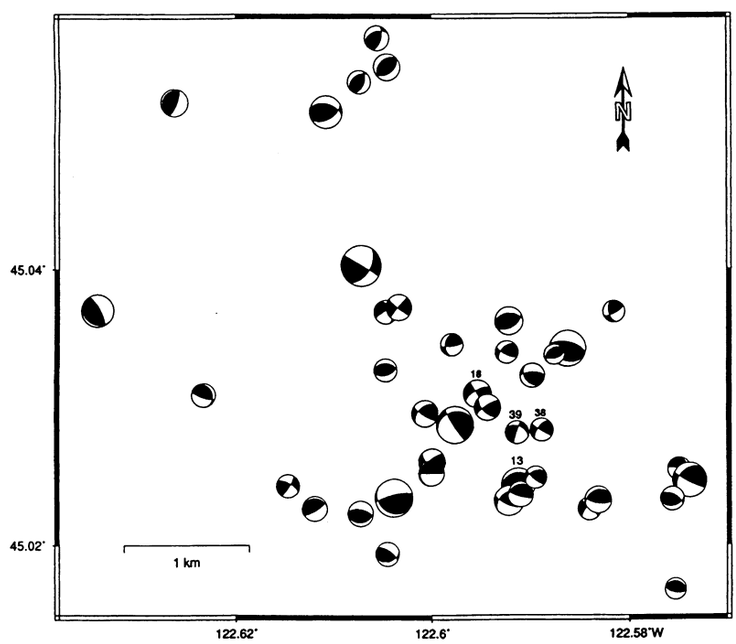

Figure 7. All 41 double-couple solutions mapped on the JHD epicentres. Beach balls are sized according to event magnitude. Lower-hemisphere projections. Events 13, 18, 38 and 39 discussed in the text are labelled.

© 1999 RAS, *GJI* 136, 000–000

gp00000771 23-12-98 08:41:03 Rev 14.05
The Charlesworth Group, Huddersfield 01484 517077

Table 2. Source parameters for 41 aftershocks of the 1993, Scotts Mills earthquake.

Ev #	OT ymd	OT hms	Lat (°N)	± (km)	Lon (°W)	± (km)	D (km)	± (km)	S/D/R (°)	P(az/pl) (°)	T(az/pl) (°)	M_w/M_d	DC (%)	PB Hz	Tr #
1	930326	073549	45.0226	.38	122.5841	.30	12.1	.44	221/70/351	179/21	86/8	1.88/1.8	95	1.0-3.0	13
2	930326	080006	45.0287	.36	122.5976	.27	12.6	.39	148/83/119	214/32	86/44	2.98/2.9	96	0.4-3.0	14
3	930326	102251	45.0255	.41	122.5749	.36	12.2	.44	13/36/186	220/38	339/32	1.84/1.7	57	1.0-5.0	17
4	930326	124523	45.0194	.35	122.6046	.28	10.7	.37	75/36/47	15/16	254/61	1.92/1.7	94	1.0-3.0	11
5	930326	125539	45.0295	.37	122.6007	.28	12.5	.43	123/78/137	180/19	74/39	2.13/2.0	84	1.5-5.0	11
6	930326	165432	45.0234	.36	122.6039	.25	11.4	.40	127/22/139	360/29	145/56	3.04/3.1	61	0.4-3.0	11
7	930326	173922	45.0403	.38	122.6072	.27	13.3	.44	32/52/2	353/24	250/27	3.23/3.1	99	0.5-3.0	13
8	930326	184348	45.0513	.35	122.6109	.27	11.2	.41	61/50/59	172/0	263/67	2.63/2.8	17	0.5-3.0	13
9	930326	195644	45.0369	.40	122.5816	.33	13.3	.48	167/53/22	119/13	19/40	1.74/1.5	70	1.0-3.0	7
10	930327	054033	45.0247	.37	122.5738	.25	12.4	.41	117/80/126	180/26	62/43	2.75/2.6	89	0.7-3.0	32
11	930327	064607	45.0520	.31	122.6263	.20	10.4	33	21/73/85	115/28	284/62	2.21/2.3	98	0.7-3.0	27
12	930327	143859	45.0343	.37	122.5863	.24	13.3	.41	118/31/103	18/15	172/74	2.91/2.9	87	0.4-3.0	26
13	930327	222416	45.0244	.35	122.5912	.25	12.1	.39	264/28/89	175/12	356/73	2.69/2.5	86	0.7-3.0	33
14	930327	233413	45.0260	.34	122.6000	.23	11.7	.36	232/73/27	1/5	94/31	2.15/1.7	52	1.0-3.0	24
15	930328	052256	45.0232	.35	122.5922	.24	12.1	.37	113/67/126	178/15	67/54	2.37/2.1	80	0.7-3.0	31
16	930328	074351	45.0237	.36	122.5910	.26	12.2	.40	247/17/53	186/31	29/57	2.00/1.8	92	1.5-3.0	30
17	930328	082007	45.0346	.38	122.5980	.27	13.1	.44	186/44/19	130/11	23/56	1.83/1.5	81	1.0-3.0	16
18	930328	085056	45.0310	.37	122.5954	.25	13.6	.40	239/69/1	196/14	102/16	2.21/1.7	99	1.0-3.0	31
19	930328	090347	45.0300	.38	122.5943	.27	13.6	.42	236/75/32	4/11	101/33	2.11/1.6	61	1.0-5.0	23
20	930328	130835	45.0249	.37	122.5895	.27	12.3	.38	130/73/129	192/19	81/48	1.75/1.1	81	1.5-3.0	14
21	930328	155036	45.0243	.36	122.6147	.25	11.4	.38	298/68/170	163/9	257/22	1.86/1.7	98	1.0-3.0	20
22	930328	232619	45.0252	.34	122.6000	.24	11.7	.36	90/87/103	168/41	13/46	2.07/1.4	77	1.0-3.0	28
23	930329	001631	45.0363	.38	122.5922	.25	13.5	.42	61/49/73	163/3	264/77	2.26/2.0	98	0.8-3.0	38
24	930329	021939	45.0233	.36	122.5832	.25	11.9	.39	98/68/105	176/21	32/64	2.14/2.0	98	0.7-5.0	19
25	930329	103959	45.0223	.35	122.6073	.25	11.5	.38	86/29/77	8/17	212/71	2.04/1.5	100	1.0-3.0	26
26	930329	224746	45.0545	.39	122.6046	.37	11.1	.52	55/48/98	155/6	26/80	2.12/1.9	42	1.5-3.0	10
27	930330	074330	45.0233	.40	122.5756	.27	12.1	.43	296/58/111	11/11	251/69	1.91/1.7	98	1.0-3.0	18
28	930330	091807	45.0369	.36	122.6047	.24	13.2	.40	240/83/319	190/33	295/22	1.89/1.3	51	1.0-3.0	26
29	930330	113620	45.0309	.32	122.6233	.23	11.6	.35	109/72/71	214/25	354/58	1.92/1.1	85	1.0-3.0	19
30	930330	114150	45.0373	.38	122.6034	.30	13.7	.42	219/87/8	354/4	84/7	2.09/1.7	76	1.0-3.0	17
31	930330	164048	45.0534	.34	122.6075	.23	11.2	.36	233/42/116	125/6	233/72	1.86/1.0	81	1.5-3.0	17
32	930330	165623	45.0566	.35	122.6056	.25	11.7	.39	250/45/134	130/8	234/60	2.00/1.6	79	1.0-3.0	15
33	930331	083538	45.0340	.38	122.5924	.32	13.5	.43	116/72/139	173/13	71/42	1.82/1.5	94	1.0-5.0	12
34	930331	192809	45.0323	.38	122.5898	.39	13.0	.44	268/67/59	21/16	136/57	1.95/1.8	66	1.0-3.0	14
35	930331	234359	45.0327	.35	122.6048	.24	12.5	.38	270/39/102	172/7	303/80	1.85/1.0	97	1.5-3.0	18
36	930401	041317	45.0168	.35	122.5753	.23	11.3	.39	101/63/92	190/18	15/72	1.71/1.3	75	1.5-3.0	18
37	930401	041744	45.0338	.38	122.5876	.30	13.4	.42	78/58/108	155/12	29/71	1.61/0.8	69	1.5-3.0	15
38	930401	043602	45.0283	.37	122.5889	.26	12.7	.39	122/85/152	171/16	74/23	1.84/1.2	96	1.5-3.0	16
39	930401	093915	45.0282	.36	122.5914	.24	12.5	.38	197/86/47	143/35	254/28	1.86/1.2	94	1.5-3.0	21
40	930402	162843	45.0227	.43	122.6120	.27	11.7	.41	59/74/80	157/28	314 /60	2.02/2.1	71	1.0-5.0	9
41	930406	094732	45.0370	.37	122.6341	30	10.9	.55	128/16/68	55/30	248/59	2.60/2.6	75	1.0-2.0	6

OT: origin time in UTC; D: depth. Location and origin time were determined by JHD. S/D/R: strike/dip/rake. P: azimuth and plunge of pressure axis. T: azimuth and plunge of tension axis. M_w: moment magnitude; M_d: coda magnitude. DC: double-couple percentage. PB: Passband used in inversion. Tr: number of traces used in inversion.

and thus differences in waveforms could not be caused by differences in propagation paths, but can be attributed solely to the sources. Although both earthquakes had a right-lateral strike-slip mechanism, the orientations of the nodal planes differ. The traces in Fig. 8 demonstrate that these differences are well resolved in the raw waveforms, with amplitudes and polarities differing considerably for the event pair at many stations.

To obtain an estimate of uncertainties, we perturb the strike, dip, and rake independently around the best-fitting double-couple solution and determine the increase in the variance of fit (Fig. 9). For event 13, the bounds for an arbitrary 5 per cent increase in variance are $\pm 13°$ for strike, $-8°$ to $+6°$ for dip, and $\pm 11°$ for rake. For event 18, the bounds are $\pm 8°$ for strike, $\pm 9°$ for dip, and $\pm 8°$ for rake. The significance of misfit for perturbed solutions can be determined more rigorously by a *t*-test as described by Huang *et al.* (1986). For event 18, our best model fits the data significantly better at the 95 per cent confidence level than models with strike deviating $+7°/-8°$, dip deviating $\pm 20°/-4°$ and rake deviating $+4°/-8°$. For the most part, we believe that uncertainties in the source orientation are smaller than 10°.

The influence of recording geometry

Because of the ephemeral character of the seismic network and large spread in event magnitudes, the station coverage varied greatly for most event recordings. It is therefore meaningful to learn how variations in the recording geometry affect the derived focal parameters. The good coverage of events 13 and

gp00000771 23-12-98 08:41:03 Rev 14.05
The Charlesworth Group, Huddersfield 01484 517077

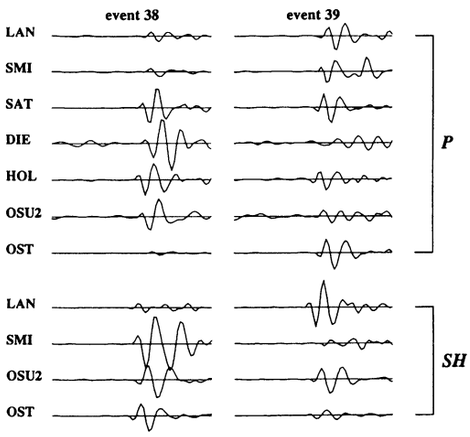

Figure 8. Observed phases for events 38 and 39 showing clear distinctions in shape, polarity, and amplitude. See Fig. 7 for locations and mechanisms of these two events.

18 allows us to investigate the effect of changes in the station geometry. We do this by decreasing the number of stations in the inversion, and by comparing the resulting fault-plane solutions with the ones derived by employing all available data (Fig. 10). First, the number of stations is reduced to five (diamonds in Fig. 10), covering a wide range of azimuth and distance. The resulting mechanism changes only slightly in source orientation (maximum change $\pm 4°$) and DC percentage. When the number of recording sites is reduced to three, well distributed around the source (circles in Fig. 10), the estimated mechanisms remain similar to the reference solutions. For both events the largest change occurs in the rake of the slip vector (8° and 11°, respectively). Finally, the spatial coverage of the remaining three stations is severely degraded (crosses in Fig. 10). The main effect for event 13 is a large increase in the CLVD part of the moment tensor, whereas the DC mechanism stays similar to the reference solution, with a maximum change of 19° in source orientation. For event 18, the DC portion stays high, and all source parameters remain within 5° of the reference mechanism. Overall, the mechanisms are robust towards changes in station distribution. In most inversions, more than three stations were used, usually with good coverage around the source. Only event 41 had the same, one-sided coverage, as the last test realization for event 13. However, this experiment shows that the DC mechanism should still be reliable.

Magnitudes

The estimated seismic moment can be converted to a magnitude scale using the relation of Hanks & Kanamori (1979). Fig. 11 compares coda-duration magnitudes (M_d) published by Thomas *et al.* (1996) and moment magnitudes (M_w) derived in this study. The correlation tying the two magnitudes together works well for larger magnitudes, but breaks down for events with $M_w \leq 2.2$, with M_d being as much as a factor of two smaller than moment magnitudes. We take the opportunity of having precise magnitude estimates to derive a corrected

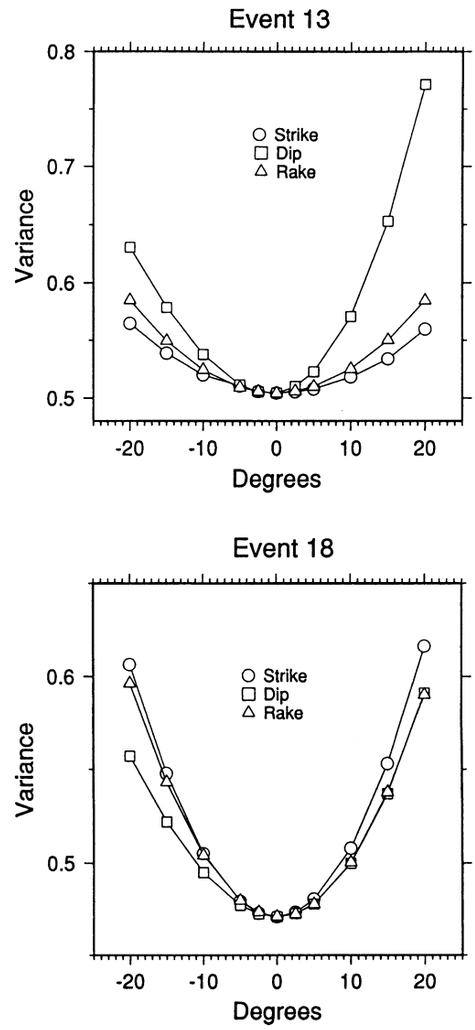

Figure 9. Normalized variance of fit for events 13 and 18 as a function of deviation from the best-fit double-couple solution for the three parameters strike, dip, and rake.

M_w–M_d relationship for events of magnitude less than 2.2. From the coda-duration magnitudes provided by Thomas *et al.* (1996) we recalculated the median coda durations using the relationship of Crosson (1972). The coda length to magnitude relationship for this sequence (Fig. 11) is best described by two line segments

$$M = \begin{cases} 0.465 + 1.059 \log(\bar{T}), & \bar{T} < 45 \text{ s} \\ -2.293 + 2.741 \log(\bar{T}), & \bar{T} \geq 45 \text{ s}, \end{cases}$$

gp00000771 23-12-98 08:41:03 Rev 14.05
The Charlesworth Group, Huddersfield 01484 517077

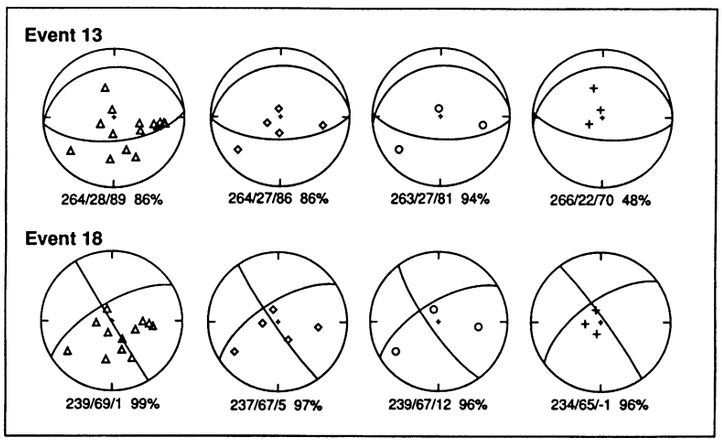

Figure 10. Double-couple solutions for events 13 and 18 derived from various station distributions. The symbols indicate projections (lower hemisphere) of the up-going rays. The first three numbers indicate strike, dip, and rake of the double-couple solution; the fourth number is the double-couple portion of the moment tensor. The derived source mechanisms are robust towards changes in station coverage.

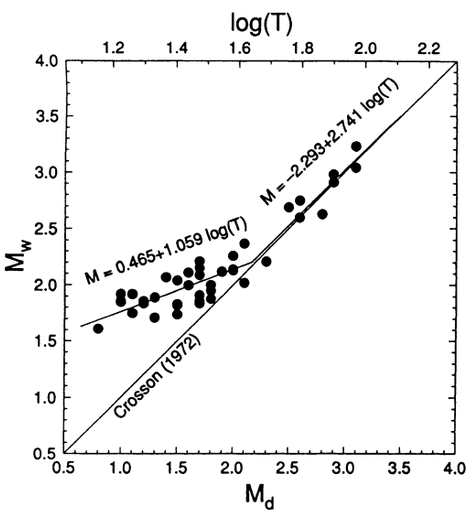

Figure 11. Graph showing the moment magnitude estimate (M_w) from the waveform inversion versus the coda-duration magnitude (M_d, lower abscissa) from Thomas *et al.* (1996). Coda durations clearly underestimate magnitudes for events with $M_w < 2.2$. Also shown is a plot of the logarithm of derived median coda duration (T, measured in seconds, upper abscissa) versus moment magnitude. The relation is best described by two line segments intersecting at $M = 2.2$. The diagonal line, when referring to log(T), is the relation found by Crosson (1972) from earthquakes in the Puget Sound area.

where $\bar{T}$ is the median coda duration. The second line is similar to the one found by Crosson (1972) (Fig. 11).

HYPOCENTRE LOCATIONS

Hypocentres were located using a two-step procedure. First, hypocentres were determined with a conventional single-event scheme from data of both the regional Pacific Northwest Seismic Network (PNSN; Ludwin *et al.* 1994) and the temporary array. While only P picks were made from the vertical instruments of the PNSN, the three-component records of the temporary network also yielded precise S arrival times. The single-event locations were used to calculate Green's functions for the moment tensor analysis and as a starting model for a joint determination of hypocentres (JHD) (Douglas 1967).

The JHD method is based on the observation that traveltime errors from an earthquake cluster are highly correlated at each station. Hence errors due to deviations from the assumed traveltime model can be expressed as a single time correction for each station. This technique has been applied to both teleseismic (for example Jordan & Sverdrup 1981) and regional studies (for example Herrmann *et al.* 1981; Pavlis & Booker 1983; Pujol 1988). Although such multi-event schemes may not yield better absolute locations, the relative positions of the earthquakes are much improved, producing a more focused picture of clustered seismicity.

In the implementation of JHD in this study, we seek station corrections for both P and S arrivals. We use a half-space with an assumed P velocity, but invert additionally for v_p/v_s ratio. Because a half-space does not bend rays or generate refracted arrivals, only stations of the temporary array, and the two closest PNSN stations SSO and VG2, are used. The linear system in this inversion problem is ill-conditioned because the station corrections are linearly dependent on origin times, if the earthquakes originate from a small region. To overcome

gp00000771 23-12-98 08:41:03 Rev 14.05
The Charlesworth Group, Huddersfield 01484 517077

this problem, we constrain the sum of P and the sum of S corrections to vanish.

The 25 stations used in the inversion are well distributed around the aftershock cluster (Fig. 12); many stations lie within one hypocentral depth of the epicentres, providing excellent depth control. The high-quality three-component recordings at most sites enabled precise picking of both P and S phases. S picks were determined from SH components to avoid complications from compressional-wave precursors. The final inverse solution yields a v_p/v_s ratio of 1.78 for a half-space P velocity of 5.5 km s^{-1}, and reduces the cumulative RMS residual almost tenfold, from 0.3508 to 0.0364 s. Estimates of location uncertainties, obtained from the *a posteriori* model parameter covariance, are on average 320 m for the epicentres and 410 m for depths (Table 2). The *a posteriori* standard deviation of the data weighted by pick uncertainty is approximately 2, indicating that the errors are due approximately in equal parts to errors in the data (picking errors) and shortcomings of the model parametrization. Station corrections are displayed in Fig. 12. A marked change from negative corrections to large positive corrections is perceptible across the toe of the Cascade Mountains (east of the 300-m contour). This is partly due to topography, which was inadequately corrected for by the chosen half-space velocity.

A map showing JHD relocations and the shift from the original single-event locations is displayed in Fig. 13(a). The coordinates of the JHD locations are given in Table 2. JHD moves the events in the cluster to the southeast and closer together. A group of four earthquakes in the north and some scattered events in the east become more isolated from the main cluster. Fig. 13(b) shows cross-sections perpendicular to the strike of a best-fitting plane through the events before and after relocation, and Fig. 13(c) shows the projection on the best-fitting plane.

The single-event locations are scattered, and although the cross-section reveals a trend, it is not well resolved. In contrast, most of the relocated events collapse to a well-focused plane. This result is quite surprising, considering the multitude of nodal plane orientations derived earlier (Fig. 7). The strike and dip of the plane are tightly constrained, and only four events to the north and two events in the northwest are clearly separated from it. Disregarding these six events, the best-fitting plane found by multivariate least-squares regression has a strike of $283 \pm 4°$ and a dip of $49 \pm 4°$ (uncertainties are 95 per cent confidence limits). The two events at the bottom left (events 18 and 19) are the only events to be located more than one standard deviation away from the best-fitting plane.

STRESS-FIELD CONSIDERATIONS

Assuming a pervasively fractured crust, the average directions of pressure (P) and tension (T) axes, averaged over a large number of earthquakes, are expected to approximate the directions of the principal stresses σ_1 (maximum) and σ_3 (minimum), respectively. Background seismicity in the Pacific Northwest appears to occur for most part under a NS compressional stress field (Crosson 1972, 1983; Ma *et al.* 1991). This direction of maximum regional compressive stress has also been confirmed by borehole breakouts in NW Oregon (Werner *et al.* 1991). In Fig. 14(a) a composite plot of P- and

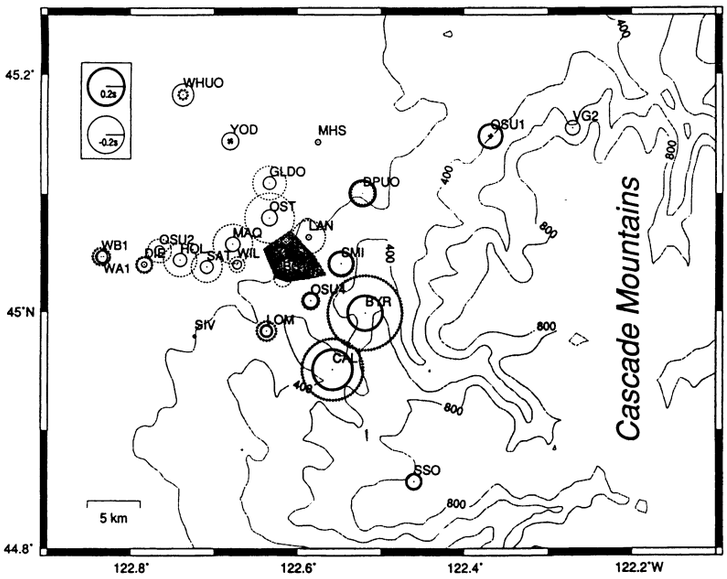

Figure 12. Map of all stations, with station corrections superimposed as circles with their radii proportional to the correction time. Solid lines are P corrections, dashed lines are S corrections—thick lines depict positive and thin lines negative values. The shaded area indicates the epicentral region of the aftershocks. For display purposes, contours above 800 m in the Cascade Mountains are not drawn.

gp00000771 23-12-98 08:41:03 Rev 14.05
The Charlesworth Group, Huddersfield 01484 517077

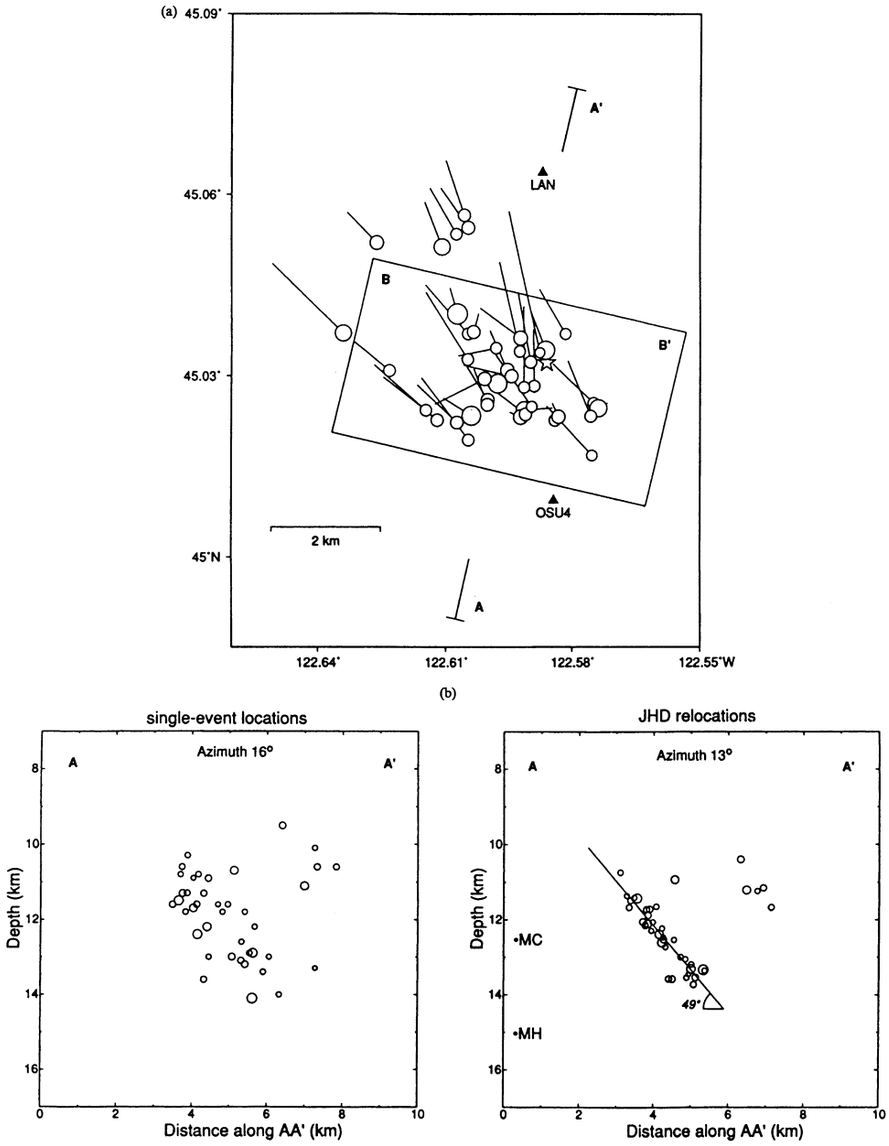

Figure 13. (a) Map of JHD relocations (circles are scaled according to event magnitude). The lines point to the original single-event locations. The bars A and B locate the surface projection of the cross-sectional planes shown in parts (b) and (c). (b) Vertical cross-sections of hypocentres perpendicular to a best-fitting plane before (left) and after (right) relocation. MH and MC labels indicate published estimates of the main shock's hypocentral (Thomas *et al.* 1996) and centroid (Nábělek & Xia 1995) depths, respectively. A rough minimum estimate of the fault width ruptured during the main shock is provided by the formula 2(MH-MC)/sin(dip). (c) The aftershocks that define the plane are shown projected onto that best-fitting fault plane. Values on the abscissa are arbitrary and shown only to indicate relative distance. Symbols denote mechanism style: circles predominant thrust, diamonds predominant strike-slip, circled pluses oblique slip. The dashed line encircles the estimated main-shock rupture area. The exact location of the main-shock slip is not known, and the circle is arbitrarily centred inside the cluster.

gp00000771 23-12-98 08:41:03 Rev 14.05
The Charlesworth Group, Huddersfield 01484 517077

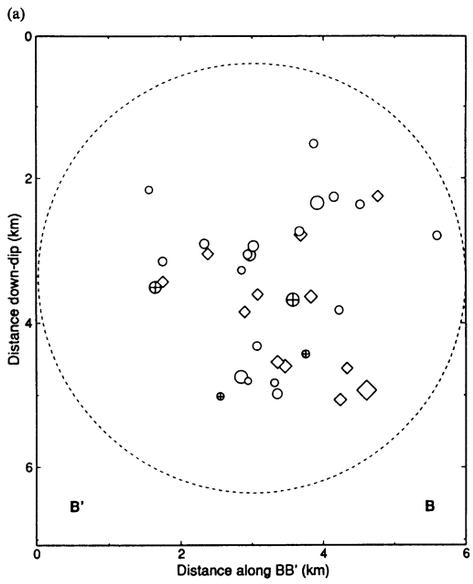

Figure 13. (*Continued.*)

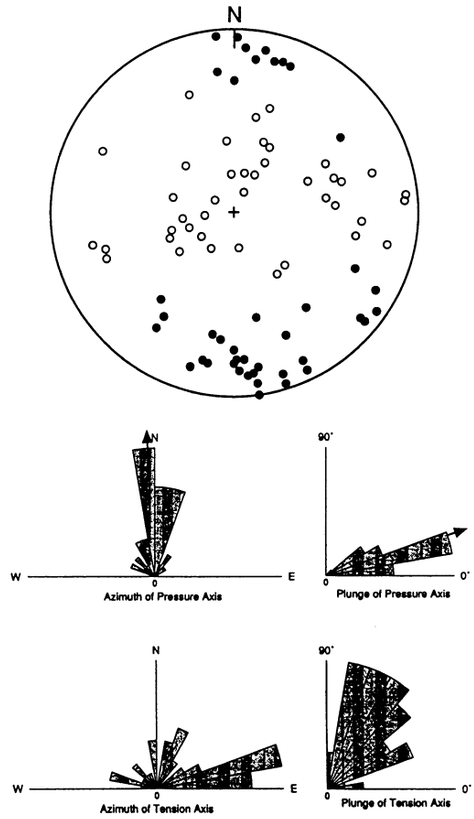

Figure 14. Composite plot of *P*-axes (filled circles) and *T*-axes (open circles) from all derived moment tensors. Bottom: Normalized rose-section diagrams showing the distribution of azimuths and plunges in 10° increments. Note the uniformly aligned *P*-axes and the widely distributed plunges of *T* axes. The arrow indicates average direction of the *P*-axes.

T-axes from the 41 moment tensors for the Scotts Mills aftershock sequence is shown. Below the stereo-net projection, azimuths and plunges are binned in 10° sectors and displayed in normalized rose diagrams. Their distribution displays a much greater dispersion for *T*-axes than for *P*-axes. *P*-axes reveal an approximately horizontal, N–S maximum compressive stress. *T*-axes are roughly evenly distributed on a great circle with E–W azimuth, and their plunges range from subvertical to subhorizontal. Their distribution shows no preference for either strike-slip or thrust mechanisms, indicating an approximately uniaxial stress field with $\sigma_1 > \sigma_2 \approx \sigma_3$ at that depth range. Very similar distributions have been found in general seismicity studies in the Pacific Northwest (Crosson 1972, 1983; Ma *et al.* 1991; Wang *et al.* 1995), yet it is surprising that this pattern is mimicked by the aftershocks.

Fig. 15 shows all focal mechanisms in a *T*-axis plunge versus depth graph that separates strike-slip events to the left and dip-slip events to the right. There appears to be a systematic change of deformation style as a function of depth. Even though there is significant scatter, and measurements are only over a small depth range, a trend from deeper strike-slip events to shallower dip-slip events is perceptible. To emphasize this relationship, *T*-axis plunges were binned in three depth slices and displayed in a sector diagram (Fig. 15, right). The rotation of the *T*-axes with depth is now more obvious, and average values of about 60° for events shallower than 12 km, 45° for events between 12 and 13 km, and 30° for events deeper than 13 km are obtained. A similar relationship, although in the extensional regime of the Basin and Range province, was reported by Vetter & Ryall (1983). They attributed the change from primary strike-slip motion for shallow events to the oblique or dip-slip motion of deeper events to increasing overburden pressure. We too attribute the rotation of the tension axis for the Scotts Mills aftershocks to increasing overburden pressure. That the rotation is perceptible over such a small depth range can be attributed to the fortuitous circumstance that the depth where $\sigma_2 \approx \sigma_3$ is approximately in the middle of the aftershock range.

DISCUSSION

Aftershocks are commonly thought to occur as a response to static stress increases induced by the main-shock dislocation. The predicted stress concentrations are highest at the fault ends or, in the case of a heterogeneous rupture, in the areas around patches of large slip, which consequently most often become the site of aftershock concentrations (for example Das

gp00000771 23-12-98 08:41:03 Rev 14.05
The Charlesworth Group, Huddersfield 01484 517077

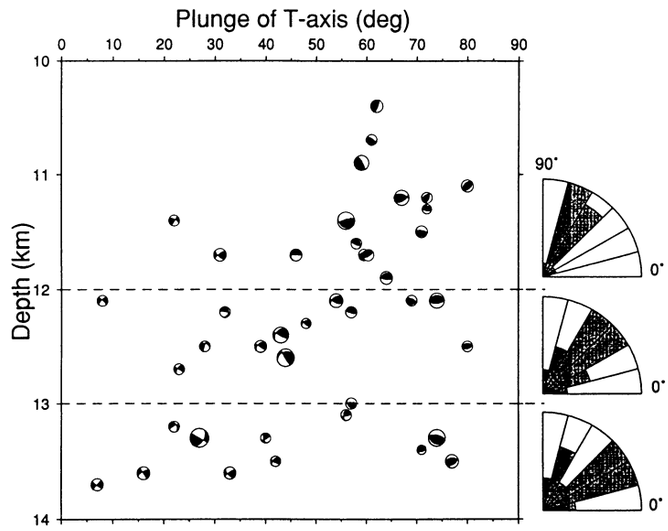

Figure 15. Left: Graph of *T*-axis plunge versus hypocentral depth. Actual double-couple estimates (beach balls, scaled by M_w) are used as symbols. In this plot, strike-slip mechanisms plot on the left and dip-slip mechanisms on the right. Right: Rose diagrams of *T*-axis plunge. The data are binned into three depth slices. *T*-axis plunges rotate from an average of 60° to an average of 30° with increasing depth.

& Scholz 1982; Bakun *et al.* 1986; Mendoza & Hartzell 1988; Nábělek & Suarez 1989; Oppenheimer *et al.* 1990; King *et al.* 1994). Significant increases in Coulomb stress can also occur in dilatational lobes on the sides of the main-shock slip plane. Although aftershocks can occur on conjugate fault planes (for example Bowman *et al.* 1990), generally we expect them to have similar fault-plane solutions to the main shock. This is particularly true when the main shock does not entirely relieve the deviatoric regional stress (King *et al.* 1994).

For the Scotts Mills earthquake, estimates of the orientation of the preferred main-shock slip plane vary from 294° to 302° for the strike and from 48° to 58° for the dip in the three published solutions (Nábělek & Xia 1995; Thomas *et al.* 1996). A similar plane was defined by the aftershocks (283°, 49°), suggesting that the events outline the main-shock rupture surface. The aftershocks adjoining the rupture plane are relatively evenly distributed over an area of approximately 20 km^2 (Fig. 13c). Nábělek & Xia (1995) estimated the main-shock's rupture area to be approximately 28 km^2 (dashed circle of 3 km radius in Fig. 13c) from the source duration, assuming a circular crack model. Unfortunately, a detailed slip distribution for this earthquake is not available. Nevertheless, an upward rupture can be indirectly inferred from the difference between the nucleation depth, determined from regional short-period *P* waves (15.1 km; Thomas *et al.* 1996; MH in Fig. 13b), and the centroid depth, representing the average depth of moment release from waveform modelling (12–13 km; Nábělek & Xia 1995; MC in Fig. 13b). All aftershock depths are shallower than the main-shock hypocentre for the single-event locations and the JHD relocations (Fig. 13b), as well as for the locations published by Thomas *et al.* (1996), placing them within the zone that slipped during the main shock (Fig. 13c).

Six events to the northwest of the cluster are clearly separated from the major plane (Fig. 13b). Five of them (events 8, 11, 26, 31, and 32) form a group of relatively shallow, northeast-striking, dip-slip events. Their clustering and similarity in mechanism (Fig. 7) suggest that they are located on a single, separated plane to the north of the major fault plane. This conclusion is supported by their NW–SE-trending compression axes, which differ from the mostly N–S-trending axes of the events forming the major plane. Similar off-fault seismicity has been reported for numerous strike-slip earthquakes (for example Das & Scholz 1982; King *et al.* 1994).

The most enigmatic feature of this earthquake sequence is that the majority of events seem to sharply define a plane, although their focal mechanisms are extremely diverse. Because almost none of the mechanisms has a nodal plane that agrees with the probable main-shock fault plane (Fig. 7), the aftershocks cannot have occurred on the main-shock slip plane, but must have ruptured tightly around it on adjacent, secondary structures. We found other characteristics of the Scotts Mills sequence that defy explanation by generic aftershock models. The aftershocks seem to respond to a uniform stress field that closely resembles the ambient regional tectonic stresses. This conclusion is substantiated by a change from dip-slip to strike-slip deformation with depth, which is appealingly explained by increasing overburden pressure, but which can only with difficulty be main-shock-induced. Although detailed information on main-shock slip is not available, the aftershocks seem to parallel the main-shock rupture, and not to occur in barriers or around asperities, as would be predicted by other models.

To explain the characteristics of the Scotts Mills aftershocks we suggest that the events were driven by an ambient regional

gp00000771 23-12-98 08:41:03 Rev 14.05
The Charlesworth Group, Huddersfield 01484 517077

stress rather than by a main-shock-induced increase in static shear stress. We believe that they were triggered by a sudden decrease in strength following the main shock in the area adjacent to main-shock slip. A similar conclusion was reached by Beroza & Zoback (1993) to explain the diversity of mechanisms of the Loma Prieta aftershocks. It is known that even well-developed fault zones are surrounded by zones of pervasively fractured rock (Chester & Logan 1986). This fractal character of fault roughness makes the area predisposed towards the occurrence of aftershocks. A sudden elevation in pore pressure following main-shock slip could account for many of the observed phenomena. A discussion of these processes is beyond the scope of this paper.

We have shown that waveform inversion methods can be applied very well to small earthquakes, and are a good alternative to conventional first-motion techniques. Because they make more efficient use of the data, it is possible to obtain well-resolved solutions even if the station distribution is sparse. Simple, three-component, short-period velocity transducers are sufficient for this type of analysis. In our data set, a lower threshold on the magnitude of analysable events has not been attained, leading us to believe that earthquakes as small as $M = 1.0$ can be investigated.

ACKNOWLEDGMENTS

We benefited from thorough reviews by K. Koch, R. B. Herrmann, and S. N. Ward. This research was supported by the US Geological Survey, Department of Interior, grants 1434-94-G-2427 and 1434-HQ-96-GR-02736.

REFERENCES

Bakun, W.H., King, G.C.P. & Cockerham, R.S., 1986. Seismic slip, aseismic slip, and the mechanics of repeating earthquakes on the Calaveras fault, California, in *Earthquake Source Mechanics. AGU Geophys. Mono. 37*, pp. 195–207, eds Das, S., Scholz, C & Boatwright, J., Am. geophys. Un., Washington DC.

Beroza, G.C. & Zoback, M.D., 1993. Mechanism diversity of the Loma Prieta aftershocks and the mechanics of mainshock–aftershock interactions, *Science*, **259**, 210–213.

Bouchon, M., 1982. The complete synthesis of seismic crustal phases at regional distances, *J. geophys. Res.*, **87**, 1735–1741.

Bowman, J.R., Gibson, G. & Jones, T., 1990. Aftershocks of the 1988 January 22 Tennant Creek, Australia intraplate earthquakes: evidence for a complex thrust-fault geometry, *Geophys. J. Int.*, **100**, 87–97.

Braunmiller, J., Nábělek, J.L., Leitner, B. & Quamar, T., 1995. The Klamath Falls, Oregon, earthquake sequence: source mechanisms from regional data, *Geophys. Res. Lett.*, **22**, 105–108.

Brune, J., 1970. Tectonic stress and the spectra of shear waves, *J. geophys. Res.*, **75**, 4997–5009.

Brune, J., 1971. Tectonic stress and the spectra of shear waves: Corrections, *J. geophys. Res.*, **76**, 5002.

Chester, F.M. & Logan, J.M., 1986. Implications for mechanical properties of brittle faults from observations of the Punch Bowl fault zone, California, *Pure appl. Geophys.*, **124**, 79–106.

Crosson, R.S., 1972. Small Earthquakes, structure, and tectonics of the Puget Sound region, *Bull. Seism. Soc. Am.*, **62**, 1133–1171.

Crosson, R.S., 1983. Review of seismicity in the Puget Sound region from 1970 through 1978, in *Proc. Workshop XIV, Earthquake hazards of the Puget Sound Region, Washington*, US geol. Surv. Open-File Rep. **83–19**, 6–18.

Das, S. & Scholz, C., 1982. Off-fault aftershock clusters caused by shear stress increase? *Bull. seism. Soc. Am.*, **71**, 1669–1675.

Douglas, A., 1967. Joint epicentre determination, *Nature*, **215**, 47–48.

Dreger, D.S. & Helmberger, D.V., 1993. Determination of source parameters at regional distances with three-component sparse network data, *J. geophys. Res.*, **98**, 8107–8125.

Dziewonski, A.M., Chou, T.-A. & Woodhouse, J.H., 1981. Determination of earthquake source parameters from waveform data for studies of global and regional seismicity, *J. geophys. Res.*, **86**, 2825–2852.

Dziewonski, A.M., Frantzen, J.E. & Woodhouse, J.H., 1983. Centroid-moment tensor solutions for April–June, *Phys. Earth planet. Inter.*, **33**, 243–249.

Hanks, T.C. & Kanamori, H., 1979. A moment magnitude scale, *J. geophys. Res.*, **84**, 2348–2350.

Herrmann, R., Park, S. & Wang, C., 1981. The Denver earthquakes of 1967–1968, *Bull. seism. Soc. Am.*, **71**, 731–745.

Huang, P.Y., Solomon, S.C., Bergman, E.A. & Nábělek, J.L., 1986. Focal depths and mechanisms of Mid-Atlantic ridge earthquakes from body wave inversion, *J. geophys. Res.*, **91**, 579–598.

Jordan, T.H. & Sverdrup, K.A., 1981. Teleseismic location techniques and their application to earthquake clusters in the South-Central Pacific, *Bull. seism. Soc. Am.*, **71**, 1105–1130.

King, G.C.P., Stein, R.S. & Lin, J., 1994. Static stress changes and the triggering of earthquakes, *Bull. seism. Soc. Am.*, **84**, 935–953.

Koch, K., 1991a. Moment tensor inversion of local earthquake data—I. Investigation of the method and its numerical stability with model calculations, *Geophys. J. Int.*, **106**, 305–319.

Koch, K., 1991b. Moment tensor inversion of local earthquake data—II. Application to aftershocks of the May 1980 Mammoth Lakes earthquakes, *Geophys. J. Int.*, **106**, 321–332.

Ludwin, R.S., Quamar, A.I., Malone, S.D., Jonientz-Trisler, C., Crosson, R.S., Benson, R. & Moran, S.C., 1994. Earthquake hypocenters in Washington and northern Oregon, 1987–1989, and operation of the Washington Regional Seismograph Network, *Washington Division of Geology and Earth Resources Information Circular 89*.

Ma, L.R., Crosson, R.S. & Ludwin, R.S., 1991. Focal mechanisms of western Washington earthquakes and their relationship to regional tectonic stress, *US Geol. Surv. Open-File Rep.* 91–441-D.

Madin, I., Priest, G., Mabey, M., Malone, S., Yelin, T. & Meier, D., 1993. March, 25, Scotts Mills earthquake—western Oregon's wake-up call, *Oregon Geol.*, **55**, 51–56.

Mao, J.W., Panza, G.F. & Suhadolc, P., 1994. Linearized waveform inversion of local and near-regional events for source mechanisms and rupturing processes, *Geophys. J. Int.*, **116**, 784–798.

Mendoza, C. & Hartzell, S.H., 1988. Aftershock pattern and mainshock faulting, *Bull. seism. Soc. Am.*, **78**, 1438–1449.

Nábělek, J., 1984. Determination of earthquake source parameters from inversion of body-waves, *PhD thesis*, MIT, Cambridge.

Nábělek, J. & Suarez, G., 1989. The Goodnow earthquake in the Central Adirondacks, New York: rupture of a simple, circular crack, *Bull. seism. Soc. Am.*, **79**, 1762–1777.

Nábělek, J. & Xia, G., 1995. Moment-tensor analysis using regional data: application to the 25 March 1993, Scotts Mills, Oregon, earthquake, *Geophys. Res. Lett.*, **22**, 13–16.

Oppenheimer, D., Bakun, W.H. & Lindh, A.G., 1990. Slip partitioning of the Calaveras fault, California, and prospects for future earthquakes, *J. geophys. Res.*, **95**, 8483–8498.

Pavlis, G.L. & Booker, J.R., 1983. Progressive Multiple Event Location (PMEL), *Bull. seism. Soc. Am.*, **73**, 1753–1777.

Pujol, J., 1988. Comments on the joint determination of hypocenters and station corrections, *Bull. seism. Soc. Am.*, **78**, 1179–1189.

Ritsema, J. & Lay, T., 1993. Rapid source mechanism determination of large ($M_w \geq 5.5$) earthquakes in the western United States, *Geophys. Res. Lett.*, **20**, 1611–1614.

gp00000771 23-12-98 08:41:03 Rev 14.05
The Charlesworth Group, Huddersfield 01484 517077

Saikia, C.K. & Herrmann, R.B., 1985. Application of waveform modeling to determine focal mechanisms of four 1982 Miramichi aftershocks, *Bull. seism. Soc. Am.*, **75**, 1021–1040.

Saikia, C.K. & Herrmann, R.B., 1986. Moment tensor solutions for three 1982 Arkansas swarm earthquakes by waveform modeling, *Bull. seism. Soc. Am.*, **76**, 709–723.

Schwartz, S.Y., 1995. Source parameters of the 1991 Costa Rica and 1992 Cape Mendocino, California, earthquakes from inversion of local amplitude ratios and broad band waveforms, *Bull. seism. Soc. Am.*, **85**, 1560–1575.

Sileny, J., Panza, G.F. & Campus, P., 1992. Waveform inversion for point source moment tensor retrieval with variable hypocentral depth and structural model, *Geophys. J. Int.*, **109**, 259–274.

Thomas, G.C., Crosson, R.S., Carver, D.L. & Yelin, T.S., 1996. The 25 March Scotts Mills, Oregon, earthquake and aftershock sequence: spatial distribution, focal mechanisms, and the Mount Angel Fault, *Bull. seism. Soc. Am.*, **86**, 925–935.

Vetter, U.R. & Ryall, A.S., 1983. Systematic change of focal mechanisms with depth in the Western Great Basin, *J. geophys. Res.*, **88**, 8237–8250.

Wang, K., Mulder, T., Rogers, G.C. & Hyndman, R.D., 1995. Case of low coupling stress on the Cascadia subduction fault, *J. geophys. Res.*, **100**, 12907–12918.

Werner, K.S., Graven, E.P., Berkman, T.A. & Parker, M.J., 1991. Direction of maximum horizontal compressional in western Oregon determined by borehole breakouts, *Tectonics*, **10**, 948–958.

gp00000771 23-12-98 08:41:03 Rev 14.05
The Charlesworth Group, Huddersfield 01484 517077